PHYSICAL REVIEW E **72**, 041923 (2005)

Density functional theory approach for coarse-grained lipid bilayers

Laura J. Douglas Frink* and Amalie L. Frischknecht
Sandia National Laboratories, Albuquerque, New Mexico 87185, USA

(Received 18 October 2004; revised manuscript received 7 July 2005; published 25 October 2005)

Lipid bilayers are important inhomogeneous fluid systems that mediate the environment of cells and the interaction of cells with their environment. A variety of approaches have been taken to model the lipid molecules in bilayers, from all atom molecular dynamics to rigid body liquid crystals. In this paper we discuss the application of a density functional theory approach that treats the lipid molecules at the coarse-grained level of a freely jointed chain. This approach allows for compressibility effects, and can therefore be used to study not only the long range structure in lipid bilayers, but also the nanoscale structure induced in the bilayer when the lipids crystallize or when an inclusion (e.g., an embedded protein) is present. This paper presents a detailed analysis of fluid bilayers and lamellae predicted by the theory. In particular we locate solutions with zero surface tension. We calculate the phase diagram for all possible phases with planar symmetry, including uniform macrophases. Surprisingly, we find a first-order phase transition from the lamellar phase to an isolated bilayer phase on lowering the temperature. This transition appears to be driven by solvent packing effects. A further lowering of the temperature leads to a set of highly ordered bilayers.

DOI: 10.1103/PhysRevE.72.041923 PACS number(s): 87.16.Dg, 87.15.Aa, 87.14.Cc

I. INTRODUCTION

The lipids making up cell membranes play an active role in a variety of biological processes. Many of these processes, such as the formation of lipid domains or rafts, the interactions of transmembrane proteins, and membrane fusion, occur on length and time scales inaccessible to atomistic simulations. As a result, there has been increasing interest in developing more coarse-grained models for lipid membranes. Many coarse-grained models have been developed for either molecular dynamics (MD) or Monte Carlo simulations, ranging from united-atom type models [1–3] to bead-spring [4,5] or liquid-crystalline rigid rod models [6].

Theoretical approaches that can directly calculate the equilibrium structure of model membranes can be attractive for their low computational cost and clear parsing of the critical physics. A historically important approach treats membranes as continuum elastic sheets [7]. More recently molecular level theories have been proposed. May and Ben-Shaul [8,9] studied lipid-protein interactions with a theory that described the lipids with a phenomenological free energy that included head-group repulsions, a water/membrane interfacial energy, and a contribution from the configurational entropy of the tails.

Several groups have used self-consistent field (SCF) theory to study lipid phase behavior and membranes. SCF theory is a mean-field theory that in bilayer applications typically includes van der Waals–type interactions between various species, and the configurational entropy of the lipid tails. Most often lipids are modeled as infinitely thin "threads" and the fluid is assumed to be incompressible. Leermakers and co-workers [10–12] have developed a lattice SCF theory for lipids that includes chain stiffness and anisotropic interactions between tail segments. They are able to predict a fluid to gel phase transition for their bilayers. Similar lattice SCF theories are used by other groups [13–15]. Schick and co-workers have studied lipid phase diagrams using off-lattice SCF theories [16,17].

Another class of theories is based on liquid state theories. In one extreme, Somoza and co-workers [18] neglected internal degrees of freedom of the lipids, and developed a density functional theory (DFT) for anisotropic, rigid amphiphilic molecules. They were able to calculate the structure of bilayers and micelles [18]. Lagüe and co-workers [19–21] developed an integral equation theory based on the laterally averaged response of the lipid hydrocarbon tails (obtained from atomistic MD simulations). They used the theory to calculate the potential of mean force between transmembrane proteins, modeled as rigid cylinders. However, the theory neglects the lipid head groups, the entropy of the tails, and any fluctuations normal to the bilayer.

In this paper we consider the molecular density functional theory of Chandler, McCoy, and Singer (CMS) [22–24], as extended to polymeric molecules by McCoy, Curro and co-workers [25–27]. We use the implementation first suggested by Donley *et al.* and detailed further by Frischknecht *et al.* [28–30]. The lipids are modeled as coarse-grained spherical interaction sites. Like SCF theory, the DFT is a mean-field theory and includes the energetics of hydrophobic-hydrophilic interactions and the entropy of the lipid tails. Furthermore both the SCF and our DFT approach treat the tail configurations as random walks. However, the DFT approach includes compressibility and packing effects via explicit liquid state structure as determined from an integral equation theory of polymeric molecules (polymer reference interaction site model theory). Thus the DFT includes two length scales in predicting bilayer structure, the length scale of the lipid chains, and the length scale of the beads on the chain.

We describe our model system in Sec. II and computational methods in Sec. III. We present our results for bilayer structure and phase behavior in Sec. IV. In this paper we

---

*Corresponding author: Electronic address: ljfrink@sandia.gov

1539-3755/2005/72(4)/041923(13)/$23.00

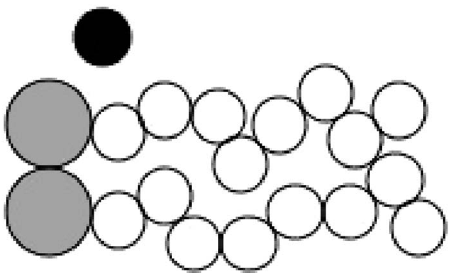

FIG. 1. A sketch of the model lipid-solvent system. The tail beads (white) and the solvent (black) are the same size. The head-group beads (gray) are larger by a factor of 1.44.

restrict our results to morphologies that vary in only one dimension, since we are primarily interested in lipid bilayers. Our implementation of the theory can, however, treat systems in two or three dimensions; an example is given in Sec. IV E where we show some preliminary results for the effect of an inclusion in the bilayer. Details of the calculations can be found in the appendixes. Finally, comparison of the DFT results found here with molecular dynamics simulations can be found in the following paper [31].

II. THE MODEL SYSTEM

Our approach is to coarse-grain the lipid molecules while retaining both the flexible nature of the tails as well as the different size and energetic characteristics of hydrocarbon tails and polar head groups. The lipid molecules consist of freely jointed, tangent spherical sites or "beads." Typical lipids found in biological systems have tails composed of 14–20 carbon atoms. There are a wide variety of head groups possible both in nature and in engineered lipid systems. In this work we focus on a specific coarse-grained lipid model in which the tails are eight beads long (roughly two CH_2 groups per bead), and the head groups are lumped into two larger beads with energetic properties different from the tail beads. This 8-2-8 model is then a linear copolymer chain, as shown in Fig. 1. The different sites in the lipid interact with standard Lennard-Jones (LJ) potentials,

$$u_{\alpha\beta}(r) = u^{LJ}_{\alpha\beta}(r) - u^{LJ}_{\alpha\beta}(r_c), \tag{1}$$

$$u^{LJ}_{\alpha\beta}(r) = \frac{4\epsilon_{\alpha\beta}}{kT}\left[\left(\frac{\sigma_{\alpha\beta}}{r}\right)^{12} - \left(\frac{\sigma_{\alpha\beta}}{r}\right)^{6}\right], \tag{2}$$

where r_c is the cutoff distance where the potential goes to zero, k is Boltzmann's constant, and T is the temperature.

We are interested in bilayer-forming lipids and thus chose the ratio of head to tail bead diameters to be $\sigma_h/\sigma_t = 1.44$, giving an overall head-group volume fraction of 0.27. On the basis of simple packing arguments and previous theoretical work on similar lipid models [17], we expect this ratio to result in lamellar and bilayer-forming lipids. In addition to the lipid molecules, the model has a single site solvent with diameter $\sigma_s = \sigma_t \equiv \sigma = 1$. We set the cross terms in the bead diameters from the usual Berthelot scaling rules, so that $\sigma_{\alpha\beta} = 0.5(\sigma_\alpha + \sigma_\beta)$. The self-assembly of the lipids into bilayers is driven by the various interactions in the system. We have chosen the tail-solvent and tail-head interactions to be purely repulsive with $r_c = 2^{1/6}\sigma_{ts}$ and $r_c = 2^{1/6}\sigma_{th}$, respectively. Solvent-solvent, solvent-head, head-head, and tail-tail interactions are all uniformly attractive with a cutoff of $r_c = 3.5\sigma$. Finally, we set all of $\epsilon_{\alpha\beta} \equiv \epsilon = 1$. This combination of parameters allows for a self-assembling bilayer to form. We note that one could choose model parameters in a more physical way to represent specific lipids, as has been done by others [11]. Here we take a general approach, inspired by previous coarse-grained MD simulations [4,5] and SCF theories [16,17], and explore the predictions of the DFT for this initial simple model. We will report all lengths in units of σ and energies in units of ϵ/kT.

III. METHODS

The details of the CMS DFT applied here to coarse-grained lipid models, along with the numerical methods used to solve the theory, have been enumerated elsewhere [29,32]. Briefly, the basic quantity in the theory is the inhomogeneous site density profile $\rho(\mathbf{r}) = \Sigma_\alpha \rho_\alpha(\mathbf{r})$, where $\rho_\alpha(\mathbf{r})$ is the density of site type α at $\mathbf{r}$. The basic idea in CMS DFT is to replace the inhomogeneous, interacting system of interest with a reference system of ideal, noninteracting chains and solvent, in a medium induced potential $U_\alpha(\mathbf{r})$ which captures the effects of the site interactions. The theory is formulated in the grand canonical ensemble (GCE), with the grand potential free energy Ω of the inhomogeneous system of interest measured relative to the free energy Ω_b of the bulk, homogeneous lipid-solvent mixture which serves as the reservoir for the inhomogeneous system. Then the grand potential free energy difference $\Delta\Omega = \Omega - \Omega_b$ is given by a Taylor series expansion about the noninteracting reference system, truncated at second order. A functional minimization of $\Delta\Omega$ leads to the DFT equations to be solved. For completeness, we review this system of equations in Appendix A. Here we give details of the calculations presented in this paper.

A. Density functional calculations

A state point in the GCE is specified by μ_s, μ_L, V, and T where μ_s is the solvent chemical potential, μ_L is the lipid chemical potential, V is the system volume, and T is the temperature. The μ variables are defined indirectly in the CMS DFT by specifying the site number densities of solvent and lipid in a mixed bulk reservoir fluid. We report here the total site number density in the reservoir ρ_b, and the number fraction of solvent, x_s, in that reservoir.

There is no way in this grand canonical ensemble to guess *a priori* how the state variables $\{T, \rho_b, x_s\}$ should be chosen in order to obtain a bilayer structure, or furthermore to guarantee the constraint of zero surface tension that is expected for biologically relevant structures. For this work, we chose to keep the value of ρ_b fixed at $\rho_b\sigma^3 = 0.59$. We restricted our solutions to have planar symmetry so that the densities were nonuniform only perpendicular to the bilayer, and analytical integration of the two dimensions parallel to the bilayer was possible. While a homogeneous solution of mixed lipids and solvent at constant bulk density is always a stationary state of this DFT approach, it is clearly not the solution of interest. In order to obtain bilayerlike solutions, suitable initial guesses were required. Initial guesses consisting of step function density profiles were used (with some trial and error) to generate a nonuniform bilayerlike solution. Arclength continuation algorithms were used to step from one converged solution to another (see Appendix B for more details) [33]. We performed exhaustive arclength continuation calculations as a function of T and x_s to find the possible thermodynamic states of the system. Finally, bilayer states of interest (e.g., zero tension bilayers) were identified.

Most of the calculations presented here had a total computational domain size of 40σ with reflecting boundary conditions on either side of the domain. Reflecting boundaries assume $\rho_{B+i}=\rho_{B-i}$ where B is the node at the boundary, i is an integer, and ρ is any variable in the calculation. For single bilayer solutions, we often locate the center of the bilayer at one of the reflecting boundaries. This ensures symmetric bilayer solutions, and removes any numerical instabilities due to drift of bilayer-solvent interfaces in the computational domain. Note that in this case the reflecting boundaries result in a periodic stack of bilayers with neighbors separated by 80σ. This separation is always large enough to ensure that neighboring bilayers are independent.

B. Properties of bilayers

Lipid bilayers are inhomogeneous fluids with soft boundaries. An extensive literature exists that describes the physics of fluids at hard boundaries [34]. Much of the analysis from those physical systems can be transferred directly to bilayers with the caveat that the Gibbs dividing surface may be trickier to define. In general, the properties of interfacial fluids are defined by the excess surface free energy [see Eq. (A9) for the particulars of our theory]. The excess surface free energy Ω^{ex} is the free energy difference between the bilayer-solvent system of interest and a pure solvent. The pure solvent density needed to calculate Ω^{ex} is not known *a priori*, but is observed as the solvent density far from the bilayer in any inhomogeneous solution. This excess free energy is also precisely the surface tension, γ,

$$\gamma=\Omega^{ex}=\frac{\{\Delta\Omega[\rho(\mathbf{r})]-\Delta\Omega^{s}\}}{A}, \tag{3}$$

where $\Delta\Omega^s$ is the difference in free energy between the pure solvent and the bulk homogeneous reservoir, and A is the total area.

Equation (3) is an energetic route to the surface tension. It is also possible to use a mechanical route to compute the surface tension [35],

$$\gamma=\int_{-\infty}^{\infty}dx\, s(x)=\int_{-\infty}^{\infty}dx[P_N(x)-P_T(x)], \tag{4}$$

where the stress profile across the bilayer is $s(x)=P_N(x)-P_T(x)$, x is the direction normal to the bilayer, $P_N(x)$ is the normal component of the pressure tensor (a constant for all x as dictated by mechanical equilibrium), and $P_T(x)$ is the tangential component of the pressure tensor. Thermodynamically, the grand free energy density $\Omega(x)/V$ can be identified with the lateral pressure $P_T(x)$ [36,37], and thus a stress profile is rather straightforward to compute with DFT (see Appendix A for a precise derivation).

The basic structural quantities that define a given bilayer are the bilayer thickness t and the density of lipids in the bilayers, usually reported as the area per lipid A_L. Reported thicknesses are given as the distance between head-group density peaks, while A_L is calculated from

$$A_L=(\Gamma_L/A)^{-1}\equiv\left(N_\alpha^{-1}\int\rho_\alpha(x)dx\right)^{-1} \tag{5}$$

where $\rho_\alpha(x)$ is the density profile of any single site type α on the lipid and Γ_L is the total number of lipid molecules in the system.

IV. RESULTS

While the coarse-grained model presented in Sec. II seems quite simple, the complexity of the solution space is significant. Appendix B details this complexity, along with computational strategies for locating solutions of interest. We begin this section with a description of the most biologically relevant bilayer structures that we find in the model. We then go on to explore the phase diagram of our model in more detail.

A. Bilayer structure

In biological membranes, the surface tension is expected to be zero. The $\gamma=0$ bilayer for our model at the state point $kT/\epsilon=1.3$ and $\rho_b\sigma^3=0.59$ is shown in Fig. 2(A). The density profile across the bilayer has tail beads in the inner part of the bilayer, head groups clustered at the bilayer-solvent interface, and solvent excluded from the bilayer. The density profiles do not exhibit significant packing structure indicating that the bilayer is in a fluid state. This zero tension bilayer is not the only solution of the DFT found for this model at this state point. Rather, a whole series of solutions are obtained with different integral numbers of bilayers in the computational domain (see Appendix B). Eventually the space is completely filled with a lamellar state as is shown in Fig. 2(B).

We can compare the structure of our model bilayers to experiment by a rough mapping of the coarse-grained model. The ratio of head-group volume to tail volume in our lipid is similar to that in dipalmitoylphosphatidylcholine (DPPC); if we assume that the volume of one of our tail beads is equivalent to two CH_2 groups in DPPC, we can identify $\sigma=4.75$ Å. Here we have used a volume of 28.1 Å^3 for the CH_2 groups in DPPC [38]. We can then compare the thicknesses of our bilayers, measured as the distance between the head group density peaks, and the areas per lipid with values in the literature. For fully hydrated DPPC at 50 °C, the head-to-head distance $t=38.3$ Å and the area per lipid $A_L=64$ Å^2 [39]. These conditions should apply to our fluid bilayers at zero tension. Using our mapping for σ, we find that the thickness for bilayers in this model varies from 38 to 35.2 Å

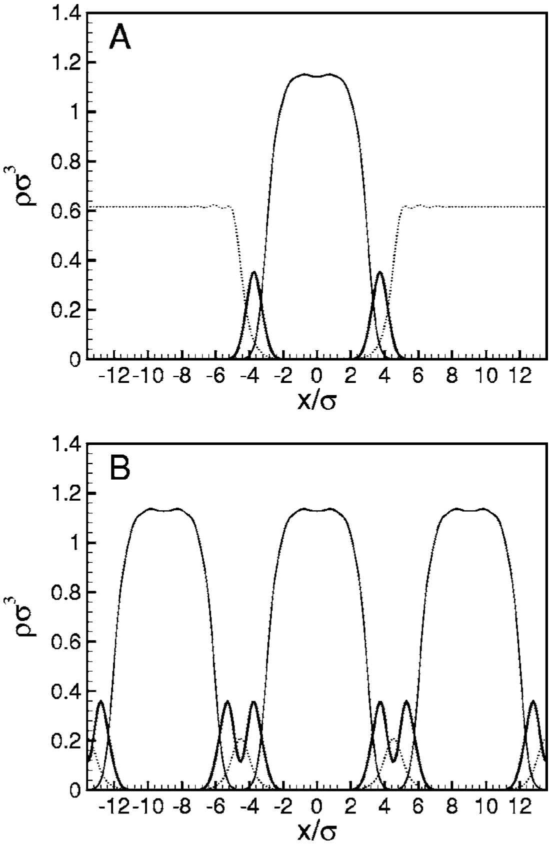

FIG. 2. Density profiles for zero tension bilayers, showing the head groups (bold solid curve), tail groups (solid curve), and solvent (dotted curve). The two cases shown are a single isolated bilayer (A), and a lamellar stack (B). The lamellar profile has a repeat period of $\lambda=9.05\sigma$. The distance between head-group peaks on either side of the bilayers is found to be 7.4σ for the isolated bilayer and 7.5σ for the lamellar bilayers. The state point for both profiles is $\{x_s=0.415, \rho_b\sigma^3=0.59, kT/\epsilon=1.3\}$.

and the area per lipid from 77.4 to 110.3 Å^2 for zero tension bilayers where the temperature ranges from $kT/\epsilon=0.92$ to 1.3. The best fit to the DPPC data is thus at low temperatures in the model, close to the transition to ordered bilayers (see below). While arguments could be made for making adjustments to the model (adding stiffness or changing coarsening strategy), and while we have limited this analysis in phase space by constraining $\rho_b\sigma^3=0.59$, we nevertheless see that this model does predict bilayers with properties reasonably close to experimental lipid bilayers.

In addition to stacked bilayers, we find that the model exhibits a morphology where two bilayers are fused. Figure 3 shows these fused bilayers at the zero tension point for the assembly. In this case some of the tails leak out beyond the head groups, fusing the two bilayers together. Note that the chemical potential of the $\gamma=0$ point for the fused assembly is different than the chemical potential for the $\gamma=0$ point of the independent bilayers described above.

While zero tension bilayers are clearly important, a variety of experiments on bilayers or self-assembled monolayer analogs are performed at nonzero tension. The DFT approach can be used to study expected structural variations in the lipid bilayers away from the zero tension point. Figure 4 shows two extremes in lipid structure when the bilayer is under either tension [Fig. 4(A)] or compression [Fig. 4(B)]. These two extremes in structure were found at turning points located using arclength continuation algorithms (see Appendix B).

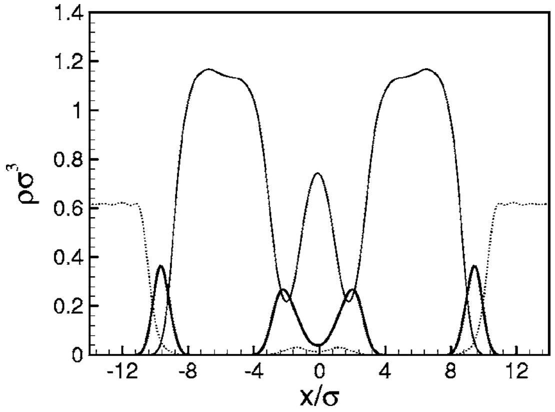

FIG. 3. Density profile for two fused bilayers at zero tension at the state point $\{kT/\epsilon=1.3, \rho_b\sigma^3=0.59, x_s=0.465\}$ (curves as in Fig. 2).

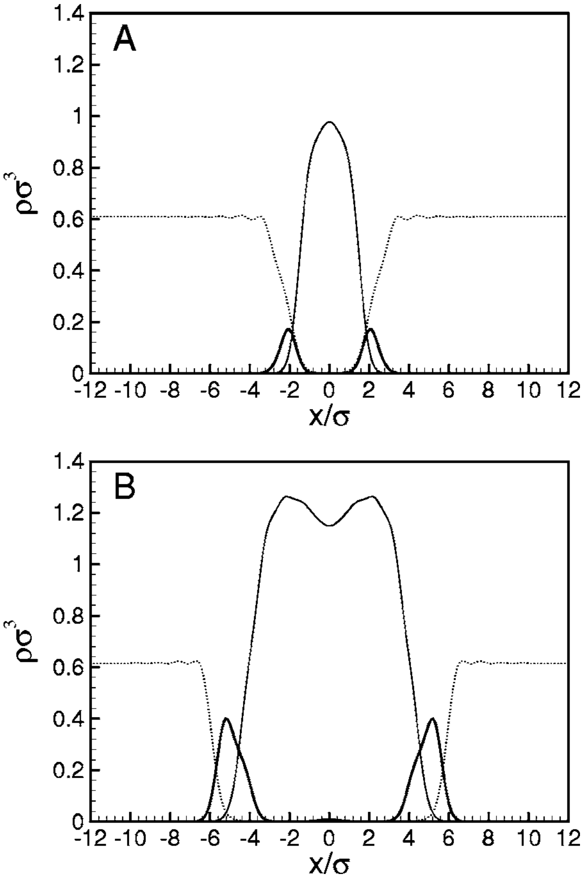

FIG. 4. Density profiles for lipid bilayers at the two extremes of stability for $kT/\epsilon=1.3$ and $\rho_b\sigma^3=0.59$. The solvent fractions and surface tensions at the two extremes are $x_s=0.303$, $\gamma=0.036kT/\sigma^2$ (A) and $x_s=0.627$, $\gamma=-0.300kT/\sigma^2$ (B) (curves as in Fig. 2; note that these two states are the two extremes of the one-bilayer curve shown in Fig. 15).

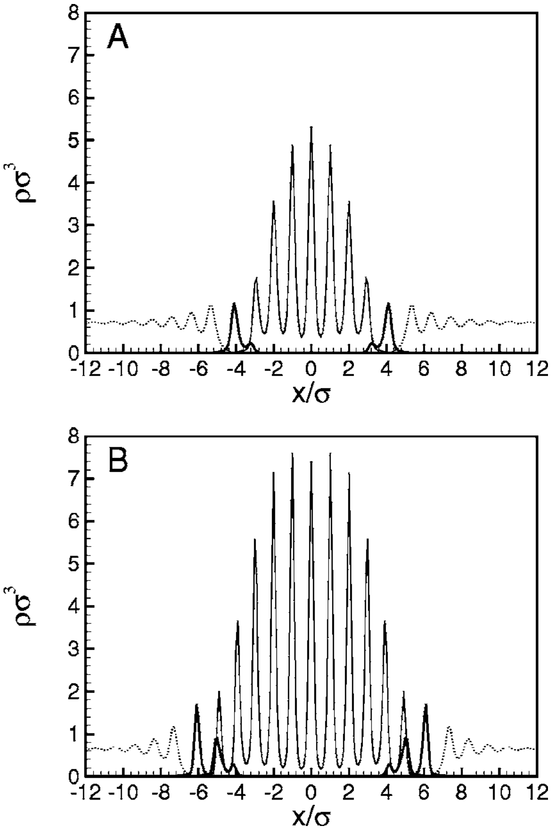

FIG. 5. Density profiles for two ordered bilayers. The narrow bilayer in (A) was found at $\{kT/\epsilon=0.877, x_s=0.3, \rho_b\sigma^3=0.59\}$. The thicker bilayer in (B) was found at $\{kT/\epsilon=0.943, x_s=0.668, \rho_b\sigma^3=0.59\}$ (curves as in Fig. 2).

At low temperatures we obtain bilayers with strongly ordered tails from the DFT. As with the fluid systems, the thickness of the bilayers varies with state point. In this case, we observe an increasing number of ordered peaks as the bilayers become wider. Figure 5 shows two examples of ordered profiles. While this order-disorder transition may be akin to the main gel transition observed in real lipid systems, we note that in contrast to experiments, the character of the transition observed here is continuous (discussed further below). Furthermore while experimental gel phases are characterized by nearly fully extended lipid chains, we never observed fully separated leaflets with 16 peaks in the DFT calculations.

The characteristics of our ordered states likely arise from the flexibility in the chains. Previous theoretical SCF descriptions of the gel phase required the inclusion of both some stiffness in the lipid tails and an anisotropic packing interaction [10,40,41]. Our DFT does include packing effects and since the theory is nonlocal (in contrast with SCF theories), one may expect that some anisotropy can arise in highly ordered profiles. However, the large entropy associated with flexible chains hinders the formation of gel phases; previous CMS DFT studies of polyethylene required some chain stiffness in order to obtain a freezing transition [42]. Thus the ordered phases predicted by our theory are likely driven by packing effects.

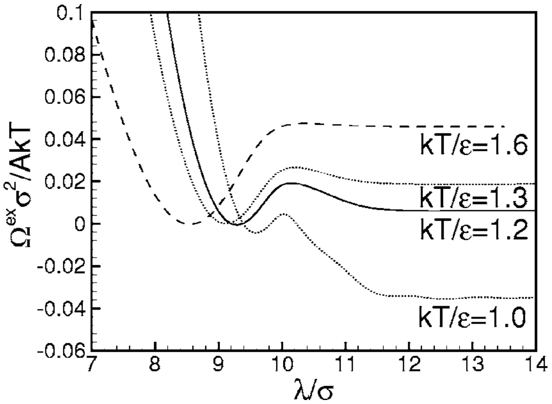

FIG. 6. Excess surface free energy as a function of the period of a uniform stack of bilayers for different temperatures, all with the lamellar phase at zero tension.

B. Bilayer hydration

As is clear from Fig. 2, these model systems can exhibit variable amounts of bilayer hydration. The structure of bilayers is generally studied experimentally by considering multilamellar assemblies, and using x-ray scattering to measure precise peak positions. Thus it is quite important to understand bilayer hydration, and any possible transitions from independent bilayers to interacting lamellar assemblies.

In order to investigate the nature of different hydration states, we considered a computational domain with periodic boundaries that contained only one bilayer in an infinite stack. The size of the computational domain was varied in order to determine whether there is a preferred hydration state with minimal free energy. A first-order phase transition requires that there will be a free energy barrier between competing hydration states that have the same free energy at the same state point. Thus the repeat period of the stack, λ is the order parameter of interest.

Figure 6 shows Ω^{ex} as a function of λ for several $\{T, x_s, \rho_b\sigma^3=0.59\}$ state points where the lamellar morphology is at $\gamma=0$. There are clearly two competing thermodynamic phases with an energy barrier in between them in all of the curves [43]. At large λ, Ω^{ex} becomes a constant indicating that the bilayer is fully hydrated and independent of neighboring bilayers. In an infinite system, the observed spacing between bilayers will depend only on the amount of solvent in the system. The local minima at smaller λ correspond to the lamellar morphologies. Figure 6 shows that lamellar morphologies are stable at high temperatures, and independent bilayers are stable at low temperatures. Given the free energy barrier between these two states, the point where the free energies are the same $(kT/\epsilon \approx 1.154)$ locates a first-order phase transition. This transition occurs at the $\gamma=0$ point for both the lamellar and bilayer phases where a pure solvent is also stable. Thus this transition occurs at a triple point.

The distinct nature of these two phases is apparent when bilayer properties such as the area per lipid and bilayer thickness are plotted as a function of the order parameter λ. The properties of the lamellar phase are quite sensitive to the order parameter while the properties of independent bilayers are not. Generally, A_L increases and the bilayer thickness t decreases with decreasing λ in the lamellar phase. Finally, we note that on increasing λ the bilayer structure is fixed (with A_L and t becoming constant) before the total free energy is minimized in the independent bilayer phase. We conclude that the free energy maximum that differentiates the lamellar and bilayer phases is primarily due to solvent packing effects in this model.

Although this phase transition from a lamellar to an independent bilayer phase as the temperature is lowered is a sort of unbinding transition, it is not the usual unbinding transition discussed in the literature. Elastic membrane theoretical studies have suggested that on increasing temperature in the L_α phase, steric undulations should dominate and unbinding from a lamellar stack to isolated bilayers will occur in a continuous fashion [44]. The transition found here is by contrast first order and occurs with decreasing temperature. Since our calculations are based on a mean-field theory, unbinding transitions due to steric undulations are not possible, and the membranes are in some sense infinitely rigid. However, an "anomalous" swelling regime has been documented in experiments where on decreasing the temperature toward the main (e.g., fluid to gel) transition, the lamellar spacing increases nonlinearly [45,46]. This trend is in the same direction as the predictions of the current theory where we have found that solvent packing effects are important. It remains to be seen whether this is an artifact of our coarse-grained model or has broader implications for the experimental systems.

C. Phase diagrams

The previous sections present bilayer structures and discuss hydration of bilayers in the context of biologically relevant structures at zero tension. In this section we take a broader perspective to discuss the phase behavior of the particular coarse grained model presented here. Clearly at high enough temperatures, macroscopic mixing must occur, and so there are limits to the existence of the microstructures presented previously.

In order to construct phase diagrams, it is necessary to identify all possible thermodynamic phases, and then locate coexistence curves as a function of appropriate state parameters. We have identified four distinct fluid phases and a series of ordered phases. On the fluid side we have the independent bilayer and lamellar microphases presented above, and two macrophases consisting of a solvent rich homogeneous solution and a lipid rich homogeneous solution (SRM and LRM, respectively).

The phase diagram in the $\{T, x_s\}$ plane for the case where $\rho_b\sigma^3=0.59$ is shown in Fig. 7. At very high temperatures (not shown), all species are mixed in a uniform homogeneous phase. There is a high temperature critical point (also not shown in the plot) at $\{kT/\epsilon \approx 11, x_s \approx 0.75\}$, above which the system is mixed, and below which the system phase separates into a SRM and a LRM. An example of an interface between the LRM and SRM as calculated in the DFT is shown in Fig. 8. In this particular density profile, the total spatial extent of the LRM is quite small, and so interfacial oscillations are seen throughout the lipid rich domain.

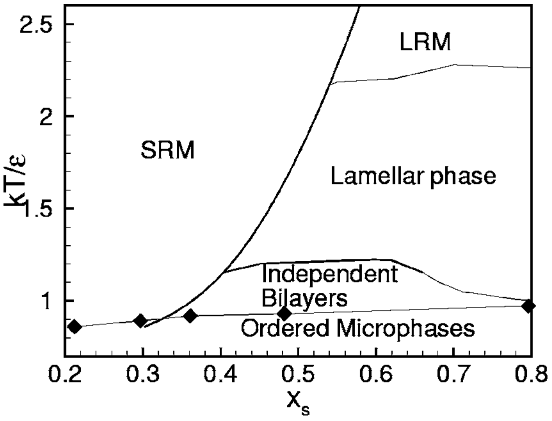

FIG. 7. Phase diagram in the T-x_s phase space.

As the temperature is lowered further, the lipids are able to self-assemble into the microphase-separated states. As discussed above, there is first a lamellar phase, followed by an independent fluid bilayer phase at lower temperatures. The surface tension is zero along the coexistence lines between the region of the SRM and either type of microphase, and a triple point occurs at $\{kT/\epsilon=1.154, x_s=0.404\}$. Another triple point is found at $\{kT/\epsilon=2.15, x_s=0.527\}$ at the coexistence point of the SRM, the LRM, and the lamellar microphase. The SRM-bilayer line enters the ordered regime continously at $\{kT/\epsilon \approx 0.91, x_s=0.33\}$. In addition this plot shows several critical points at low temperature that mark the termination of various otherwise first order layering transitions found for ordered bilayers.

The nature of the transition between the fluid and ordered bilayers is further demonstrated in Fig. 9. In essence, first-order phase transitions between bilayers with different numbers of peaks in the tail region were found at low temperature. The two-phase envelopes for several of these ordering transitions are shown in the figure. The area per lipid A_L is an order parameter much like density for liquid-vapor transitions; the plot shows pairs of data where each pair is found at the same state point and excess surface free energy, but has different morphology. As the temperature is increased, these

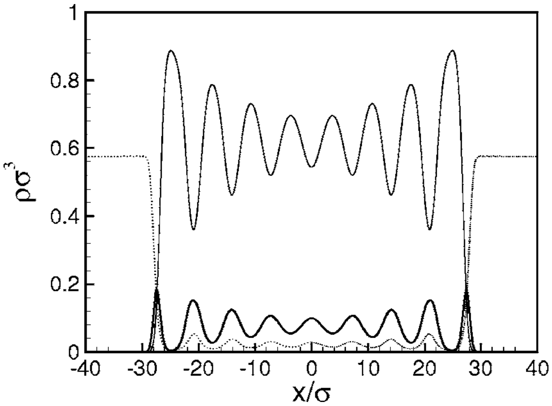

FIG. 8. Density profiles demonstrating properties of the interfaces between coexisting lipid rich and solvent rich macrophases at $kT/\epsilon=2.2$ and $x_s=0.5312$.

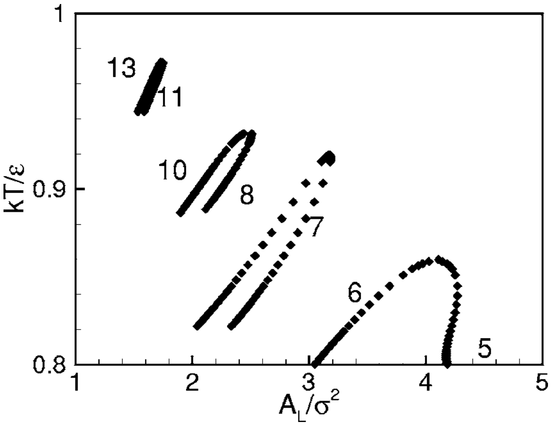

FIG. 9. Four different phase envelopes between different ordered phases exhibiting different numbers of peaks in the tail region of the bilayer density distribution.

ordering transitions terminate in critical points as the phase envelopes close. We note that phase transitions between ordered phases with six and seven peaks as well as ten and eleven peaks were found, but the complete phase envelopes were not computed.

Figure 10 shows arclength continuation calculations using both the chemical potential variable x_s and the temperature as the continuation variables. The lack of discontinuities in the temperature continuation data further confirms that the transition from fluid to ordered bilayer phases in this theory is continuous (second order). The chemical potential continuation results highlight the first-order transitions among different ordered phases, demonstrating that there are multiple solutions at many state points, and that various phases exhibit hysteresis beyond the thermodynamic transitions. As was discussed previously, stiffness in real lipid systems may preclude the complexity observed here for the ordered phases.

Finally, in order to facilitate comparison with experiment and other theoretical approaches in closed ensembles, we have generated a phase diagram in ϕ_s-T space where ϕ_s is the number fraction of solvent particles in the solution computed via

$$\phi_s = \frac{\Gamma_s}{\Gamma_L + \Gamma_s}. \tag{6}$$

For incompressible models such as those used in self-consistent field theories [17], this number fraction could be easily converted to a volume fraction.

Figure 11 shows this representation of the phase space. This plot was generated by taking several points along the coexistence curves in Fig. 7. At each point, the solvent number fractions of the two coexisting phases were computed. The solvent fractions for the independent bilayer phase were computed based on the λ of minimal hydration. This λ was established by computing Ω^{ex} as a function of λ as was done in Sec. IV B. The properties of the lamellae were also found from the small λ minima in these Ω^{ex} vs λ curves.

We see that at higher temperatures, there is a region of pure lamellae at low solvent fractions, and a region of two-phase coexistence between lamellae and an excluded SRM phase at higher ϕ_s. This behavior is seen experimentally for aqueous lipid solutions, in which there is a limit to how much a lamellar phase can be swollen, and beyond which one has a maximally hydrated lamellar phase coexisting with excess water [39]. At lower temperatures and low ϕ_s, lamellae are again found. Then with increasing ϕ_s, we find lamellae-bilayer mixtures, pure independent bilayers, independent bilayers swollen with excess solvent, and eventually pure solvent at $\phi_s \approx 1$.

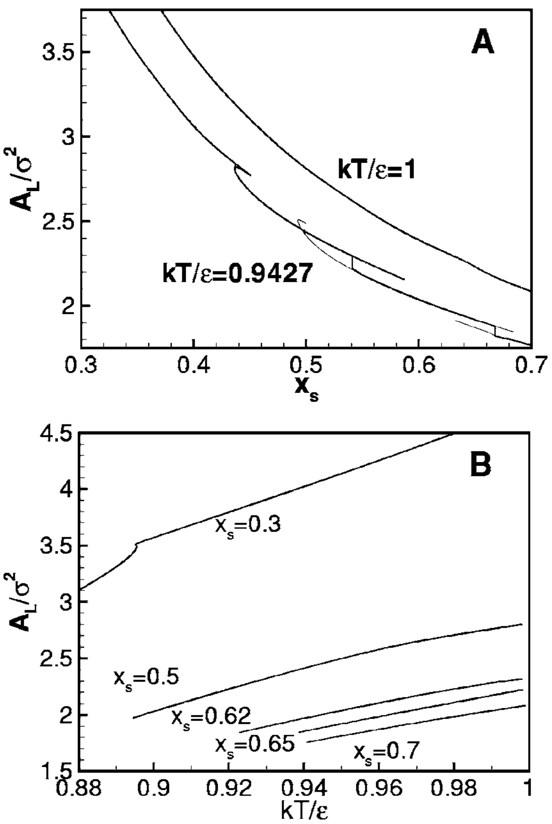

FIG. 10. Arclength continuation calculations highlighting the nature of the ordered phases exhibited by this model and theory. First-order transitions are highlighted by the $kT/\epsilon = 0.9427$ isotherm in (A) where multiple solutions are shown at many state points and hysteresis (dotted lines show metastable branches) is found around thermodynamic transitions. The continuous nature of the order-disorder transition is shown in (B) where arclength continuations in temperature at several x_s show no discontinuities.

Since we have limited our calculations to planar assemblies, our phase diagrams do not show three-dimensional morphologies (e.g., the hexagonal phase) discussed by others. Nevertheless, we can make some comparisons with previous work. Both Müller and Schick [16] and Li and Schick [17] used SCF theory to compute phase diagrams for lipid-like models. In the former case a single tailed model was used while in the latter case a double tailed lipid was studied. Both studies found a lamellar phase in a relatively large region of the phase diagram for low ϕ_s. In the work of Li and Schick, the shape of the boundary between lamellar and solvent-lamellar two phase regions was similar to the shape of the coexistence curve in Fig. 11.

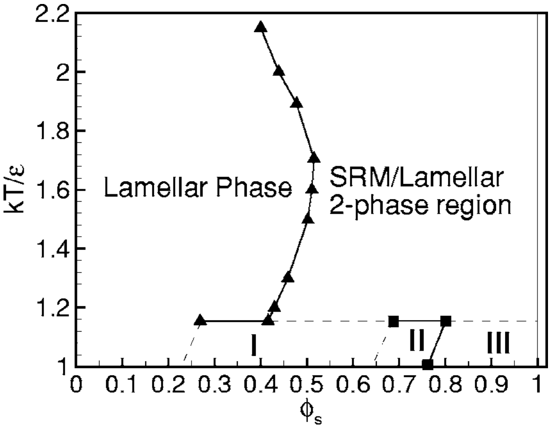

FIG. 11. Phase diagram in the ϕ_s-T space. Lamellar and two-phase lamellar-SRM regions are marked. The pure SRM phase is found on the line $\phi_s \approx 1$. Regions I, II, and II were not fully resolved, and only solid lines are based on data obtained from calculations. Nevertheless it is clear that at these low temperatures, from left to right there will be a pure lamellar phase, a mixture of lamellar and independent bilayers (region I), pure bilayers with minimal hydration (region II), swollen bilayers that take up excess solvent (region III), and finally the SRM.

D. Thermodynamic stability of fused bilayers

In Fig. 3 we showed a profile for two fused bilayers. Given the above energetic analysis, it is natural to inquire about the thermodynamic stability of two fused bilayers relative to two stacked bilayers. Figure 12 shows the free energy difference between these two cases at three temperatures along the $\gamma=0$ coexistence curve (see Fig. 7). In all cases the free energy of the fused state is higher than that of the stacked bilayers, although the fused system becomes relatively more stable at higher temperatures. This model then indicates that fused states are metastable and they would exist as fluctuation driven phenomena. For this model thermal fluctuations could be expected to be sufficient to observe fusion at higher temperatures. However, higher temperatures would also correspond to bilayers exhibiting increased undulations (not captured in the present theory) so further investigation of the interplay between fused states and undulation is required.

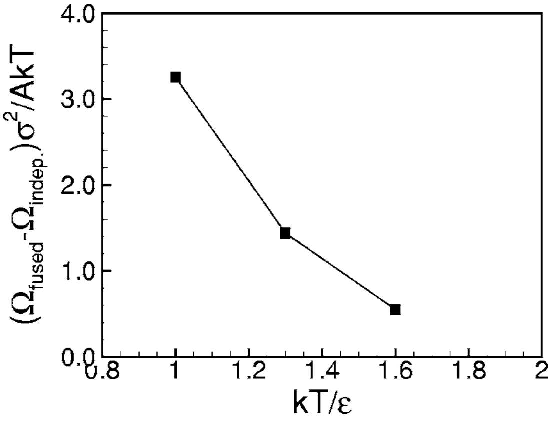

FIG. 12. Free energy difference between stacked bilayers and fused bilayers as a function of temperature.

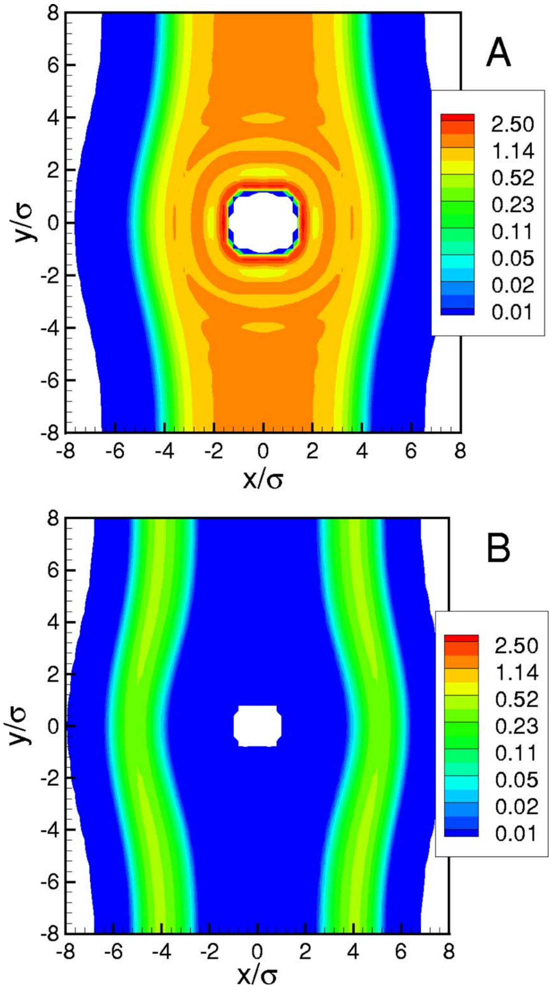

FIG. 13. (Color online) Density distributions of (A) tail segments and (B) head segments in the vicinity of a rodlike inclusion. Note that the white regions are where the respective densities of the two species are less than $\rho\sigma^3 = 10^{-8}$.

Much of the literature on fusion is currently concerned with determination of the structures that form when biological membranes fuse. The density profiles presented here do not give insight into the three-dimensional structure, but do demonstrate that fused structures are a natural observation in DFT calculations of the coarse-grained models considered here.

E. Inclusions in bilayers

Finally we note that one of the strengths of this DFT approach in comparison with other theoretical approaches applied to study lipid bilayers is that it can capture both nanostructure and mesostructure associated with inclusions in the lipid bilayer. As a demonstration, we have performed a two-dimensional calculation where a rodlike inclusion was inserted in the model bilayer. Figure 13 shows both the tail density distribution and the head-group density distribution around this inclusion. Clearly, the bilayer bends to accommodate this large object. In addition, complex structure is found within the tail region of the bilayer near the inclusion.

Although beyond the scope of this paper, various effects of the inclusion on the bilayer could be calculated from the DFT, such as the elastic length scale associated with the decay of perturbations away from the inclusion [47], or the details of the tail configurations and packing near the inclusion. While these results are preliminary, they demonstrate that this approach may be viable for investigation of a number of complicated phenomena, from hydrophobic matching to the interactions of membrane-bound proteins.

V. SUMMARY

In this paper we present in detail the behavior of a density functional theory approach to lipid bilayers based on a particular (8-2-8) coarse-grained model. We demonstrated that this theoretical approach may be suitable for studying bilayers as reasonable density profiles (tail groups to the center of the bilayer, head groups at the tail-solvent interface, and solvent excluded from the bilayer) are found. Furthermore, calculated properties for fluid bilayers (thickness and area per lipid) agree reasonably well with experimental systems at zero tension. At low temperatures, the model predicts ordered bilayers in contrast to earlier work using self-consistent field theories on flexible chain lipids. This suggests that the observed ordering results from packing effects not present in the SCF approach.

In addition to studying zero tension bilayers, we considered bilayer hydration, and more generally the phase diagram of bilayer morphologies that vary only perpendicular to the bilayer. We found that there is a first-order phase transition from a lamellar phase with low hydration to an independent bilayer phase with potentially large hydration on lowering temperature. This cannot be the unbinding transition previously studied in theoretical investigations, but it may be related to anomalous swelling observed in experiments. We find that this effect is related to solvent packing.

While this particular model may not ultimately be the ideal choice for studying a particular lipid-solvent system, the computational techniques and fundamental groundwork (including observation of fluid and ordered phases, and elucidation of the model phase diagram) provide a fundamental building block for further investigations of different lipid models, proteins interacting with bilayers, more complete physics (e.g., charged bilayers or lipid mixtures), and improved density functionals.

ACKNOWLEDGMENTS

We thank John Curro, John McCoy, Mark Stevens, and Andrew Salinger for helpful discussions. Sandia is a multiprogram laboratory operated by Sandia Corporation, a Lockheed Martin Company, for the United States Department of Energy under Contract No. DE-AC04-94AL85000. This work has been supported by the Sandia LDRD program.

APPENDIX A: SYSTEM OF EQUATIONS

1. Density functional theory

As explained briefly in Sec. III, the basic idea in CMS DFT is to replace the inhomogeneous, interacting system of interest with a reference system of ideal, noninteracting chains and solvent, in a medium induced potential $U_\alpha(\mathbf{r})$ which captures the effects of the site-site interactions. This unknown field is the field required for the ideal system to ultimately have the same density distribution, $\rho(\mathbf{r}) = \Sigma_\alpha \rho_\alpha(\mathbf{r})$, as the system of interest in the *known* external field $V_\alpha(\mathbf{r})$.

The theory is formulated in the grand canonical ensemble, with the grand potential free energy Ω of the inhomogeneous system of interest measured relative to the free energy Ω_b of the bulk, homogeneous system which serves as the reservoir for the inhomogeneous system. Then the grand potential free energy difference $\Delta\Omega = \Omega - \Omega_b$ is given by a Taylor series expansion about the noninteracting reference system, truncated at second order. A functional minimization of $\Delta\Omega$ with respect to $\rho_\alpha(\mathbf{r})$ and $\mu_\alpha - U_\alpha(\mathbf{r})$ leads to

$$U_\alpha(\mathbf{r}) = V_\alpha(\mathbf{r}) - \sum_\beta \int d\mathbf{r}' c_{\alpha\beta}(\mathbf{r}-\mathbf{r}')[\rho_\beta(\mathbf{r}') - \rho_{b\beta}], \tag{A1}$$

where μ_α is the chemical potential of site type α, $\rho_{b\beta}$ is the bulk density for site type β, and $c_{\alpha\beta}$ is the direct correlation function (DCF) between the α and β site types in the bulk fluid. The direct correlation function can be calculated from liquid state theory or obtained from simulations, and essentially describes the packing and interactions between different sites in the bulk homogeneous fluid. The calculation of $c_{\alpha\beta}(\mathbf{r})$ used in this work is described below in Sec. A 2.

Equation (A1) has two unknown functions, the density distribution of interest, $\rho_\alpha(\mathbf{r})$, and the mean field $U_\alpha(\mathbf{r})$. Clearly the relationship between the two must be defined. For the single site solvent, we simply have the usual Boltzmann distribution

$$\rho_s(\mathbf{r}) = \rho_{b,s} \exp[-\beta U_s(\mathbf{r})], \tag{A2}$$

where $\beta = 1/kT$. For the ideal gas of lipids, this relationship is

$$\rho_\alpha(\mathbf{r}) = \frac{V}{N_L}\rho_{b,L}\left\langle \delta(\mathbf{r}-\mathbf{r}_\alpha)\exp\left(-\beta\sum_\gamma U_\gamma(\mathbf{r}_\gamma)\right)\right\rangle_S \tag{A3}$$

where N_L is the total number of sites in the lipid, $\rho_{b,L}$ is the lipid site density in the bulk reservoir, and the angular brackets denote a configurational integral over all possible configurations $\{\mathbf{r}\} = \{\mathbf{r}_1, \mathbf{r}_2, \ldots, \mathbf{r}_{N_L}\}$, based on the configuration probability $S\{\mathbf{r}\}$. For a single random walk chain, the configurational probability can be written as

$$S(\mathbf{r}_1, \ldots, \mathbf{r}_{N_L}) = \prod_{s=2}^{N_L} [\omega_{\alpha\beta}(\mathbf{r}_s - \mathbf{r}_{s-1})], \tag{A4}$$

where $\omega_{\alpha\beta}(\mathbf{r}-\mathbf{r}')$ is the probability of a bond of a certain length between sites of type α at $\mathbf{r}$ and type β at $\mathbf{r}'$. In this work we will consider freely jointed chains with bond lengths $\sigma_{\alpha\beta}$, for which we have

$$\omega_{\alpha\beta}(\mathbf{r}) = \frac{1}{4\pi\sigma_{\alpha\beta}^2}\delta(|\mathbf{r}| - \sigma_{\alpha\beta}). \tag{A5}$$

Given the definition for $S\{\mathbf{r}\}$ in Eq. (A4), the density distribution for sites of type α on a linear chain lipid becomes

$$\rho_\alpha(\mathbf{r}) = \frac{\rho_{b,\alpha}}{N_\alpha}\sum_{s\in\alpha}\frac{G_s(\mathbf{r})G_s^{inv}(\mathbf{r})}{\exp[-\beta U_\alpha(\mathbf{r})]}, \qquad \text{(A6)}$$

where the sum over s is a sum over all the sites of type α in the molecule, N_α is the total number of sites of type α, and G and G^{inv} are propagator functions that describe the configurational probability based on chain connectivity. The propagator functions in Eq. (A6) obey the recursion relations

$$G_s(\mathbf{r}) = \exp[-\beta U_{\alpha(s)}(\mathbf{r})]\int d\mathbf{r}'\,\omega_{\alpha\beta}(\mathbf{r}-\mathbf{r}')G_{s-1}(\mathbf{r}'), \qquad \text{(A7)}$$

$$G_s^{inv}(\mathbf{r}) = \exp[-\beta U_{\alpha(s)}(\mathbf{r})]\int d\mathbf{r}'\,\omega_{\alpha\beta}(\mathbf{r}-\mathbf{r}')G_{s+1}^{inv}(\mathbf{r}'), \qquad \text{(A8)}$$

for the $2,\ldots,N_L$ sites in the case of Eq. (A7) and the $N_L-1,\ldots,1$ sites in the case of Eq. (A8). They satisfy the "initial" conditions $G_1(\mathbf{r})=\exp[-\beta U_{\alpha(1)}(\mathbf{r})]$ and $G_{N_L}^{inv}(\mathbf{r})=\exp[-\beta U_{\alpha(N_L)}(\mathbf{r})]$. Here $\alpha(s)$ indicates the site type of bead s. Note that Eq. (A6) reduces to Eq. (A2) in the case of an atomic liquid. In our calculations, Eqs. (A1) and (A6)–(A8) for the lipid and Eqs. (A1) and (A2) for the solvent are solved simultaneously in real space on a Cartesian grid. Our numerical methods have been enumerated extensively elsewhere [29,32]; here we simply state that we have used a Newton's method approach with update dampening as required for good convergence.

The difference between the free energy of the inhomogeneous system of interest and a bulk homogeneous system is

$$\Delta\Omega = -\int d\mathbf{r}[\rho_s(\mathbf{r})-\rho_{b,s}] - \frac{1}{N_L}\sum_{\alpha\{L\}}\int d\mathbf{r}[\rho_\alpha(\mathbf{r})-\rho_{b,\alpha}] + \frac{1}{2}\sum_{\alpha\beta}\iint d\mathbf{r}\,d\mathbf{r}'\,c_{\alpha\beta}(\mathbf{r}-\mathbf{r}')[\rho_\alpha(\mathbf{r})\rho_\beta(\mathbf{r}')-\rho_{b,\alpha}\rho_{b,\beta}], \qquad \text{(A9)}$$

where the second term is summed over all lipid sites and the sum in the last term is over all species (solvent and lipid). Note that $c_{\alpha\beta}(\mathbf{r}-\mathbf{r}')$ contains the nonideal interactions of the model of interest.

The lateral pressure profile across fluid bilayers is thought to play a significant role in membrane and membrane protein function [13,48] and is also related to the curvature elasticity of the membrane, and is hence a quantity of interest (which we explore in the following paper). Based on Eqs. (3), (4), and (A9), we can identify the stress profile with the excess surface free energy density, i.e., $s(x)=\Omega^{ex}(x)$ so that

$$s(x) = -[\rho_s(x)-\rho_{b,s}] - \frac{1}{N_L}\sum_{\alpha\{L\}}[\rho_\alpha(x)-\rho_{b,\alpha}] + \frac{1}{2}\sum_{\alpha\beta}\int dx'\,c_{\alpha\beta}(|x-x'|)[\rho_\alpha(x)\rho_\beta(x')-\rho_{b,\alpha}\rho_{b,\beta}] - S, \qquad \text{(A10)}$$

where S is a constant arising from the pure solvent contribution, and the first sum is taken over the beads in the lipid. In a pure solvent $P_T\to 0$ and so S is the isotropic pressure in a pure solvent where

$$-S = (\rho_{ps,s}-\rho_{b,s}) - \frac{\rho_{s,ps}^2}{2}\int dx'\,c_{ss}(|x-x'|) - \frac{1}{2}\sum_{\alpha\beta}\int dx'\,c_{\alpha\beta}(|x-x'|)\rho_{b,\alpha}\rho_{b,\beta} \qquad \text{(A11)}$$

and $\rho_{ps,s}$ is the density of the solvent in a solution that has a pure uniform solvent.

2. Liquid state input

The direct correlation function $c_{\alpha\beta}(r)$ in Eq. (A1) is calculated using the polymer reference interaction site model (PRISM) liquid state theory with the Percus-Yevick closure [49,50]. In this work we employ a self-consistent version of PRISM theory to calculate the DCFs. In self-consistent PRISM theory, the intramolecular structure factor $\omega(k)$ is determined from a single chain Monte Carlo (MC) simulation of the system in a solvation potential which is determined essentially by the intermolecular correlations. The PRISM equation for the intermolecular correlations is solved using the determined $\omega(k)$, and then the cycle is repeated to convergence. Thus, the intramolecular and intermolecular correlations are calculated self-consistently. This PRISM-MC approach has been shown to be in good agreement with bulk molecular dynamics simulations for a variety of polymer melts [51,52]. Good agreement with simulation was also found for PRISM-MC calculations of athermal polymer solutions with a single site solvent such as we use here [53]. We note that in our work the single chain structure is not completely consistent as it is taken to be of freely jointed form in the DFT but not in the PRISM-MC calculations. A recent study of the accuracy of this combined "random walk CMS DFT" and PRISM-MC theory found good qualitative agreement with simulation for density profiles of homopolymer melts near surfaces [54].

In this work we are interested in a wide range of attractive systems, but PRISM theory is known to be more accurate for harshly repulsive systems. Therefore, we take a perturbation approach in our treatment of the intermolecular potentials and hence of the direct correlation functions. Specifically, we apply the random phase approximation (RPA) [55]. The RPA splits $c(r)$ into two parts, a short-range, repulsive core contribution and a long-range attractive contribution,

$$c_{\alpha\beta}(r) = c_{\alpha\beta}^{\text{core}}(r) - \beta u_{\alpha\beta}^{att}(r). \qquad \text{(A12)}$$

The core term c^{core} is calculated from PRISM theory using a repulsive lipid molecule with the same architecture as the molecule of interest and with purely repulsive interactions set to $u^{rep}(r)$. The long range part is taken to be directly proportional to the attractive part of the pair interaction potential $u^{att}(r)$, as is indicated above. Here we define $u^{rep}(r)$ and $u^{att}(r)$ to be

$$u^{rep}_{\alpha\beta}(r) = \begin{cases} u^{LJ}_{\alpha\beta}(r) + \epsilon, & \text{if } r \leqslant r_{min}, \\ 0 & \text{otherwise,} \end{cases}$$

$$u^{att}_{\alpha\beta}(r) = \begin{cases} 0 & \text{if } r \leqslant r_{min}, \\ u_{\alpha\beta}(r) & \text{otherwise,} \end{cases} \tag{A13}$$

where the minimum of $u^{LJ}_{\alpha\beta}$ is located at $r=r_{min}$. Note that a true Weeks, Chandler, Anderson (WCA) approximation would instead have, for $r\leqslant r_{min}$, $u^{att}_{\alpha\beta}(r)=-u_{\alpha\beta}(r_{min})$ and $u^{rep}_{\alpha\beta}(r)=u^{LJ}_{\alpha\beta}(r)+u_{\alpha\beta}(r_{min})$ [55,56]. We do not include the temperature dependence in the calculation of $c^{\text{core}}(r)$ in order to prevent the need for new PRISM calculations at every temperature and also to ensure that we remain in the harshly repulsive regime appropriate for PRISM calculations. Given this constraint of fixed $c^{\text{core}}(r)$, it would be difficult to apply the WCA approximation because then for $r\leqslant r_{min}$ some terms (specifically, solvent-solvent, head-head, tail-tail, and head-solvent) would be shifted significantly, by ϵ/kT, while the others would not be shifted at all due to their purely repulsive character ($r_c=r_{min}$). Shifting the relative interaction strengths for $r\leqslant r_{min}$ significantly affects self-assembly for these systems. However, using the approximation of Eq. (A13) is also somewhat problematic since it results in a small discontinuity at r_{min} in the $c(r)$ used in the DFT calculations. While this combination of approximations seems to work adequately for both attractive homopolymers near attractive walls and for the fluid bilayers we consider here, it still remains to completely quantify the impact of these approximations [57].

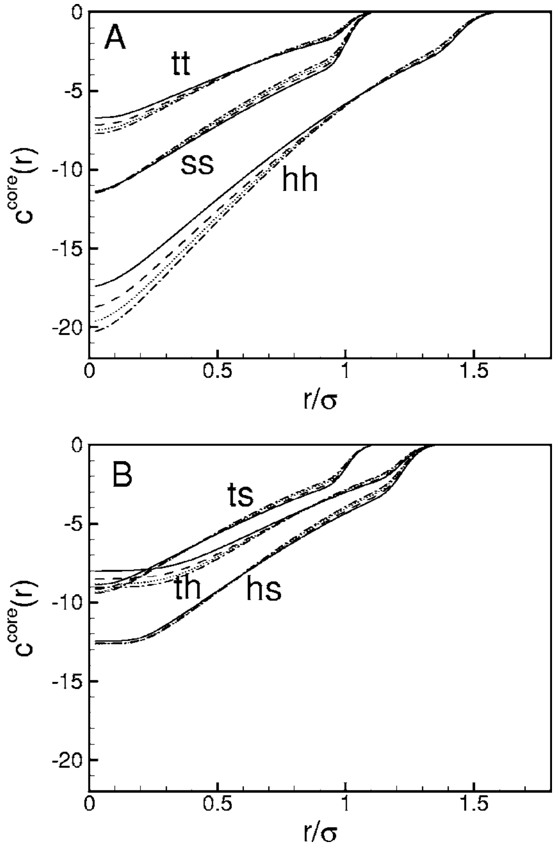

FIG. 14. Direct correlation functions for all $\alpha\beta$ pairs as a function of bulk solvent number fraction x_s at a total bulk density of $\rho_b\sigma^3=0.59$. (A) shows the direct interactions c_{tt}, c_{hh}, c_{ss} while (B) shows the cross terms c_{th}, c_{ts}, c_{hs}. Note that the subscripts indicate tail beads, head-group beads, and solvent. The various curves are for $x_s=0.001$ (solid line), 0.333 (dashed line), 0.666 (dotted line), and 0.999 (dash-dotted line) for all cases.

APPENDIX B: COMPLEXITY OF THE STATE SPACE

To locate possible solutions for the model lipid system, we applied an arclength continuation algorithm [33]. Once a solution to the DFT equations has been found, this algorithm is able to follow that solution, as a function of any continuous system parameter, along stable, metastable, or unstable solution branches and around turning (spinodal) points. This algorithm was instrumental in understanding the thermodynamic behavior of our system, since a given initial guess does not necessarily lead to the lowest free energy solution.

In order to perform these state tracking calculations, each new DFT solution requires a different $c^{\text{core}}(r)$. Since these enumerations require hundreds to thousands of solutions, it is not practical to embed the PRISM calculation within the DFT calculation. Therefore as an approximation, we typically interpolate among four $c^{\text{core}}(r)$ for a given $\rho_b\sigma^3$. For all of the calculations presented here, the four $c^{\text{core}}(r)$ functions were calculated at $x_s=0.001$, 0.333, 0.667, and 0.999. As a result, small errors can be expected at the extremes in x_s ($x_s<0.01$ and $x_s>0.99$). However, we find that most of the interesting physics occurs in the region $0.2<x_s<0.8$ where

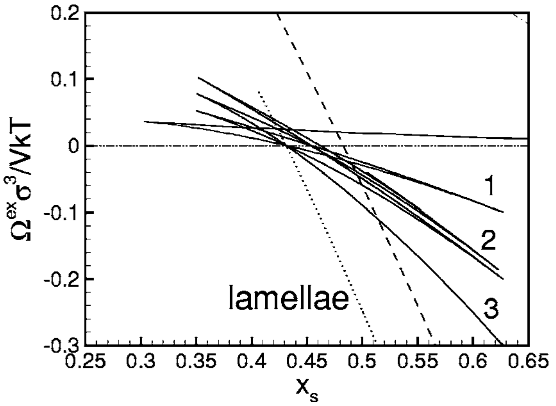

FIG. 15. Excess free energy per unit volume as a function of x_s for the state point $kT/\epsilon=1.3$ and $\rho_b\sigma^3=0.59$. The numbers in the figure indicate the numbers of bilayers in the 40σ computational domain for various branches. The various curves are as follows: bilayer solutions are shown in solid lines, space filling lamellar solutions are shown with dotted lines and are marked for clarity, a lipid rich uniform macrophase solution is shown in dashed lines, and the pure solvent solution is the dash-dot-dotted line at $\Omega^{ex}=0$.

the interpolation should be adequate. Figure 14 shows the core repulsive part of the direct correlation functions at the four chosen x_s values for all of the interactions at $\rho_b\sigma^3=0.59$ and $kT/\epsilon=1.3$. We see that the changes in $c^{\text{core}}(r)$ with concentration are relatively small for this system.

Figure 15 shows arclength continuation data at the state point $kT/\epsilon=1.3$ and $\rho_b\sigma^3=0.59$ for the excess free energy Ω^{ex} as a function of x_s. The complex solid curve has three branches that correspond to solutions with different numbers of bilayers (one, two, and three) in the computational domain. Turning points correspond to the limits of stability of the various morphologies. The branch where two bilayers are found has two parts. One corresponds to stacked bilayers, while the other corresponds to fused bilayers (see Fig. 3).

Other curves are also included in Fig. 15. The excess free energy of a solution consisting only of solvent is zero by definition [see Eq. (3)]. The lamellar data shown could not be generated by arclength continuation since the free energy for this phase must be minimized with respect to the lamellar period, i.e., the computational domain size, which in our Cartesian coordinate system is not a continuous variable. These data were thus generated by individual solves of the DFT equations. We note that zero tension assemblies occur at $\gamma=\Omega^{ex}=0$ which corresponds to a multinodal point where several branches cross in this model.

Finally, our code also includes algorithms that track binodal points in parameter space [33]. The strategy here is to solve for two solutions of differing structure simultaneously while imposing the constraint that the two solutions have identical free energies. This allows us to track binodal points, such as the multinodal point between bilayer, lamellar, and solvent solutions shown in Fig. 15, as a function of T. These binodal calculations are straightforward provided that optimization of the computational domain size is not required. So we can easily compute the coexistence curves between solvent rich and lipid rich macrophases. We can also compute coexistence between bilayers with a large excess pure solvent region and a pure solvent solution because the bilayers are not constrained by the computational domain and will find their optimal structure. This allows us to find all $\gamma=0$ bilayers as a function of temperature in our model in an automated way.

[1] J. C. Shelley, M. Y. Shelley, R. C. Reeder, S. Bandyopadhyay, and M. L. Klein, J. Phys. Chem. B **105**, 4464 (2001).

[2] C. F. Lopez, P. B. Moore, J. C. Shelley, M. Y. Shelley, and M. L. Klein, Comput. Phys. Commun. **147**, 1 (2002).

[3] S. J. Marrink, A. H. de Vries, and A. E. Mark, J. Phys. Chem. B **108**, 750 (2004).

[4] R. Goetz and R. Lipowsky, J. Chem. Phys. **108**, 7397 (1998).

[5] M. J. Stevens, J. Chem. Phys. **121**, 11942 (2004).

[6] G. Brannigan and F. L. H. Brown, J. Chem. Phys. **120**, 1059 (2004).

[7] S. May, Curr. Opin. Colloid Interface Sci. **5**, 244 (2000).

[8] S. May and A. Ben-Shaul, Biophys. J. **76**, 751 (1999).

[9] S. May and A. Ben-Shaul, Phys. Chem. Chem. Phys. **2**, 4494 (2000).

[10] F. A. M. Leermakers and J. M. H. M. Scheutjens, J. Chem. Phys. **89**, 6912 (1988).

[11] L. A. Meijer, F. A. M. Leermakers, and J. Lyklema, J. Chem. Phys. **110**, 6560 (1999).

[12] F. A. M. Leermakers, A. L. Rabinovich, and N. K. Balabaev, Phys. Rev. E **67**, 011910 (2003).

[13] R. S. Cantor, Biophys. J. **76**, 2625 (1999).

[14] M. D. Whitmore, J. P. Whitehead, and A. Roberge, Can. J. Phys. **76**, 831 (1998).

[15] M. D. Whitmore and J. P. Whitehead, Can. J. Phys. **76**, 883 (1998).

[16] M. Müller and M. Schick, Phys. Rev. E **57**, 6973 (1998).

[17] X. J. Li and M. Schick, Biophys. J. **78**, 34 (2000).

[18] A. M. Somoza, E. Chacón, L. Mederos, and P. Tarazona, J. Phys.: Condens. Matter **7**, 5753 (1995).

[19] P. Lagüe, M. J. Zuckermann, and B. Roux, Faraday Discuss. **111**, 165 (1998).

[20] P. Lagüe, M. J. Zuckermann, and B. Roux, Biophys. J. **79**, 2867 (2000).

[21] P. Lagüe, M. J. Zuckermann, and B. Roux, Biophys. J. **81**, 276 (2001).

[22] D. Chandler, J. D. McCoy, and S. J. Singer, J. Chem. Phys. **85**, 5971 (1986).

[23] D. Chandler, J. D. McCoy, and S. J. Singer, J. Chem. Phys. **85**, 5977 (1986).

[24] J. D. McCoy, S. J. Singer, and D. Chandler, J. Chem. Phys. **87**, 4853 (1987).

[25] J. B. Hooper, J. D. McCoy, and J. D. Curro, J. Chem. Phys. **112**, 3090 (2000).

[26] J. B. Hooper, M. T. Pileggi, J. D. McCoy, J. D. Curro, and J. D. Weinhold, J. Chem. Phys. **112**, 3094 (2000).

[27] J. B. Hooper, J. D. McCoy, J. D. Curro, and F. van Swol, J. Chem. Phys. **113**, 2021 (2000).

[28] J. P. Donley, J. J. Rajasekaran, J. D. McCoy, and J. D. Curro, J. Chem. Phys. **103**, 5061 (1995).

[29] A. L. Frischknecht, J. D. Weinhold, A. G. Salinger, J. G. Curro, L. J. D. Frink, and J. D. McCoy, J. Chem. Phys. **117**, 10385 (2002).

[30] A. L. Frischknecht, J. G. Curro, and L. J. D. Frink, J. Chem. Phys. **117**, 10398 (2002).

[31] A. L. Frischknecht and L. J. D. Frink, following paper, Phys. Rev. E **72**, 041924 (2005).

[32] L. J. D. Frink, A. G. Salinger, M. P. Sears, J. D. Weinhold, and A. L. Frischknecht, J. Phys.: Condens. Matter **14**, 12167 (2002).

[33] A. G. Salinger and L. J. Frink, J. Chem. Phys. **118**, 7457 (2003).

[34] *Fundamentals of Inhomogeneous Fluids*, edited by D. Henderson (Dekker, New York, 1992).

[35] J. Rowlinson and B. Widom, *Molecular Theory of Capillarity* (Oxford University Press, New York, 1982).

[36] A. J. M. Yang, P. D. Flemming III, and J. H. Gibbs, J. Chem. Phys. **64**, 3732 (1976).

[37] J. R. Henderson, in *Fundamentals of Inhomogeneous Fluids* (Ref. [34]).

[38] R. S. Armen, O. D. Uitto, and S. E. Feller, Biophys. J. **75**, 734

(1998).
[39] J. F. Nagle and S. Tristram-Nagle, Biochim. Biophys. Acta **1469**, 159 (2000).
[40] F. Schmid and M. Schick, J. Chem. Phys. **102**, 2080 (1995).
[41] F. Schmid, Phys. Rev. E **55**, 5774 (1997).
[42] J. D. McCoy, K. G. Honnell, K. S. Schweizer, and J. G. Curro, J. Chem. Phys. **95**, 9348 (1991).
[43] We note that very similar curves are seen in a SCF calculation for the interaction energy of two independent bilayers, in this case with the bilayers at zero tension, as the distance between them is reduced. In this paper the lamellar phase is not discussed, but it is shown that similar results are obtained using both a grand canonical ensemble (constant μVT) and a constant $N\gamma T$ ensemble (with $\gamma=0$). See L. A. Meijer, F. A. M. Leermakers, and J. Lyklema, J. Phys. Chem. **99**, 17282 (1995).
[44] R. Lipowsky and S. Leibler, Phys. Rev. Lett. **56**, 2541 (1986).
[45] J. F. Nagle, H. I. Petrache, N. Gouliaev, S. Tristram-Nagle, Y. Liu, R. M. Suter, and K. Gawrisch, Phys. Rev. E **58**, 7769 (1998).
[46] G. Pabst, J. Katsaras, V. A. Raghunathan, and M. Rappolt, Langmuir **19**, 1716 (2003).
[47] R. A. Kik, F. A. M. Leermakers, and J. M. Keijn, Phys. Chem. Chem. Phys. **7**, 1996 (2005).
[48] G. S. Attard, R. H. Templer, W. S. Smith, A. N. Hunt, and S. Jackowski, Proc. Natl. Acad. Sci. U.S.A. **97**, 9032 (2000).
[49] K. S. Schweizer and J. G. Curro, Adv. Polym. Sci. **116**, 319 (1994).
[50] K. S. Schweizer and J. G. Curro, Adv. Chem. Phys. **98**, 1 (1997).
[51] M. P. Pütz, J. G. Curro, and G. S. Grest, J. Chem. Phys. **114**, 2847 (2001).
[52] J. G. Curro, E. B. Webb III, G. S. Grest, J. D. Weinhold, M. P. Pütz, and J. D. McCoy, J. Chem. Phys. **111**, 9073 (1999).
[53] S. Mendez, J. D. Curro, M. Putz, D. Bedrov, and G. D. Smith, J. Chem. Phys. **115**, 5669 (2001).
[54] A. L. Frischknecht and J. G. Curro, J. Chem. Phys. **121**, 2788 (2004).
[55] J.-P. Hansen and I. R. McDonald, *Theory of Simple Liquids*, 2nd ed. (Academic Press, San Diego, CA, 1986).
[56] J. D. Weeks, D. Chandler, and H. C. Andersen, J. Chem. Phys. **54**, 5237 (1971).
[57] We note that the combination of the RPA approximation with the WCA split of the potential gives reasonably good agreement between DFT and simulation for attractive polymer systems [54]; modifying the split of the potential to that of Eq. (A13) leads to only slightly worse agreement [A. L. Frischknecht (unpublished)].